Article

Influence of Synthesis Approach on Controlled Microstructures and Photocatalytic Properties of Ag/AgBr-Activated Carbon Composites on Visible Light Degradation of Tetracycline

Saheed O. Sanni [1,2,*] , Hendrik G. Brink [1] and Elvera L. Viljoen [2]

1   Department of Chemical Engineering, Faculty of Engineering, Built Environment and Information Technology, University of Pretoria, Pretoria 0028, South Africa; deon.brink@up.ac.za
2   Biosorption and Wastewater Treatment Research Laboratory, Department of Chemistry, Faculty of Applied and Computer Sciences, Vaal University of Technology, Vanderbijlpark 1900, South Africa; elverav@vut.ac.za
*   Correspondence: saheed.sanni@up.ac.za

Abstract: The influence of the synthesis approach (thermal polyol and deposition–precipitation) regarding the dispersion of Ag/AgBr nanoparticles dispersed on activated carbon prepared from chemical impregnated pinecone (TP-AABR-ACK, and DP-AABR-ACK) was studied, to increase their photocatalytic efficiency on the degradation of tetracycline (TC). The physicochemical characterization evidenced the significance of the ACK catalyst promoter in enhancing controlled microstructures (morphologies and particle size distributions), synergistic interface interaction between AABR NPs and the carbonaceous support, and efficient photogenerated charge carriers separation within TP-AABR-ACK, and DP-AABR-ACK composites. The results revealed 92% removal of TC within 180 min under the LED visible light irradiation, which was achieved using TP-AABR-ACK when compared to DP-AABR-ACK composite and other catalysts in this study. Such superior results achieved with TP-AABR-ACK composite were attributed to controlled morphologies, reduced particle size and agglomeration, improved absorptivity, and superior cooperative effect between the AABR and ACK catalyst promoter as evidenced from SEM, EDX, TEM, UV-DRS, and electrochemical characterizations, respectively. Furthermore, enhanced TOC removal and abundance of reactive superoxide anion generation were achieved with the TP-AABR-ACK composite in this study.

Keywords: silver/silver bromide; activated carbon; controlled microstructures; tetracycline degradation; reactive oxygen species

1. Introduction

Wastewater effluents from pharmaceutical wastes has been identified as a crucial environmental issue, requiring urgent attention for removal [1]. The persistent overuse and abuse of pharmaceutical antibiotics, in the society nowadays have adverse effects on both aquatic and terrestrial organisms in the environment [2,3]. Tetracycline (TC) antibiotics are commonly employed for health purposes, due to their antibacterial and antimicrobial influence, which are very challenging to biodegrade in living organisms [3]. The removal of such organic compounds from water using conventional remediation methods still has limitations, and adequate outcomes are not achieved; hence, the need for cost-effective treatment method is required [4]. Host of water treatment technologies such as adsorption, biodegradation, and photocatalysis have been applied to overcome this environmental issue [3–5]. Semiconductor photocatalysis under the advanced oxidation processes (AOPs) is considered an effective environmentally friendly and economic treatment approach in addressing threats of pharmaceutical TC antibiotics in the environment [3,5–7]. Therefore, it is urgent for the design and development of efficient and suitable photocatalysts that can harvest the visible-light potentials of the solar spectrum, in achieving enhance removal of TC antibiotic from wastewater.

With this fact, a host of visible light active photocatalyst semiconductors have been reported [8–12]. Among these visible light photocatalysts, the nanostructures from plasmonic silver/silver halide (Ag/AgX, X = Br, Cl, or I) materials have attracted attention owing to their excellent light harvesting through Ag NPs surface plasmon resonance (SPR), and electronic attributes that advance reactive oxygen species (ROS) production [13]. In the past years, silver/silver bromide (Ag/AgBr) photocatalyst have had vast applications for environmental remediation and energy generation purposes [14,15]. Specifically, a rapid formation of AgBr nanoparticles (NPs) occurs during the synthetic process, which significantly influence the faster sprouting of the metallic silver nanoparticles (Ag NPs) at the photoinduced reduction stage [3]: hence, irregular morphologies, large particle size, and an evidence of agglomeration associated with this process; thus, lower photocatalytic activity along with lower efficiency in the production of ROS by the Ag/AgBr photocatalyst [3]. However, several synthetic processes have been utilized in controlling the morphologies and reducing the agglomeration of Ag/AgBr NPs [12,16–18]. However, a rapid recombination of the photoexcited electron–hole pairs through interaction with visible light with preceding works [3,17,18], during the photocatalysis process still persist, thus limiting their potential applications. An alternative approach is the immobilization of Ag/AgBr (AABR) NPs on an inert, and appropriate catalyst support, that controls the microstructures of AABR NPs and expedites the separation of photogenerated charge carriers.

Specifically, three-dimensional (3D) architectures are a well known catalyst support, which have attracted considerable attention owing to their unique hierarchical porous network, which found vast applications in photocatalysis [19], supercapacitors [20], and sensing [21]. The 3D network materials aid in efficient dispersion of photocatalyst NPs, enhanced visible light absorptivity, and promote fast separation of photogenerated charge carriers in semiconductor photocatalysis applications [22–24]. Particularly, the high surface area activated carbon (AC) derived from low cost, reproducible, and abundance biomass materials has formed ordered nanostructures with a host of photocatalyst materials. The 3D AC also increased intimate contact between the pollutant and active sites of photocatalyst, thus facilitating the efficient separation of charge carriers with high catalytic activities [22,25,26]. Hence, the application of activated carbon synthesized from microwave pyrolysis of pinecone chemically impregnated with potassium hydroxide (ACK), will be employed as a potential catalyst promoter/support for this study, in the controlled morphologies of AABR NPs.

Studies have shown that preparation conditions (reaction temperature, structuring directing agents, and ammonium hydroxide volume) significantly influence the unique AABR nanostructures formation during the glycothermal process [17]. As such, the AABR-ACK composites were synthesized through two methods (thermal polyol—TP-AABR-ACK, and deposition–precipitation—DP-AABR-ACK) in this study [10,11], which has never been reported so far.

In this present work, the synthetic influence of the AABR-ACK composites (analyzed using SEM, XRD, FTIR, UV-DRS, and electrochemical studies) from two different methods were carried out. The visible light photocatalytic degradation of TC antibiotic was conducted. Furthermore, the generation rate of superoxide anion radical from the as-prepared catalyst, as well comparison of active photocatalysts with other previously existing studies on TC degradation, were evaluated.

2. Results and Discussions

The crystal structures of TP-AABR-ACK, DP-AABR-ACK, DP-AABR, and TP-AABR are comparatively presented as shown in Figure 1. Furthermore, the center cubic phase of AgBr depicts the peaks at about 26.6°, 31.1°, 44.3°, 54.8°, 64.8°, 73.4° that aligns with the diffraction of the (111), (200), (220), (222), (400), (420) planes of AgBr with JPCDS file: 079-0148. The Ag NPs (JCPDS file: 071-3762) [27] revealed four diffraction peaks at around 38.2°, 44.2°, 64.4°, and 77.8°, which were all assigned to (111), (200), (220), and (311) planes of Ag, [28] respectively. In addition, the peaks of metallic Ag and AgBr, for

the AABR-ACK nanocomposites, shifted by 0.2°, thus being attributed to the interfacial interaction between the AABR nanoparticles and ACK catalyst support [29–31]. These attributes for TP-AABR-ACK and DP-AABR-ACK nanocomposites will further promote fast separation of photogenerated charge carriers, thus resulting in high catalytic activities on the removal of TC antibiotics.
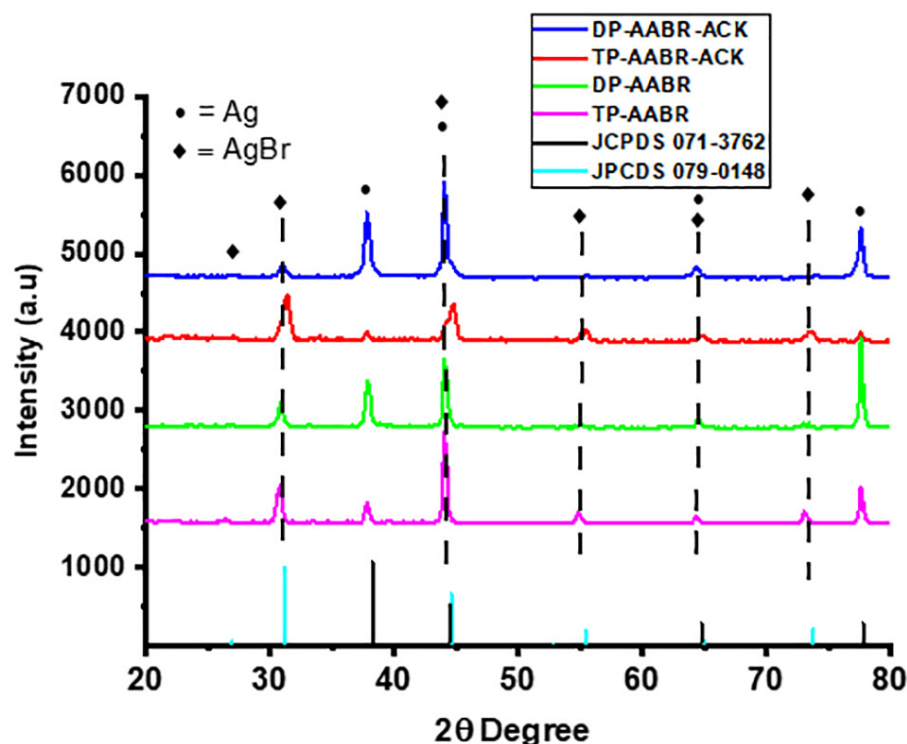

Figure 1. XRD patterns of DP-AABR-ACK, TP-AABR-ACK nanocomposites, DP-AABR, and TP-AABR.

The SEM micrographs of plasmon TP-AABR, TP-AABR-ACK, DP-AABR, and DP-AABR-ACK catalysts are presented in Figure 2a–f; herein, the morphologies of TP-AABR, and DP-AABR are irregular morphologies, agglomerated with large particle size distribution (1.2–1.7 μm) as presented in Figure 2a,d. From the SEM image for TP-AABR-ACK, and DP-AABR-ACK in Figure 2b,e, ordered nanospheres (TP-AABR-ACK) and near spheres (DP-AABR-ACK) of AABR particles are homogeneously dispersed on ACK with a significant reduction in particle size distribution to around 200–350 nm, respectively. The TP-AABR-ACK composite evidenced no agglomeration and a lower particle size diameter (Figure 2b,c) compared with DP-AABR-ACK with some slight agglomeration (Figure 2e,f). The TP-AABR-ACK composite with a minuscule particle size diameter and nanospheres morphology will thus possess a speedier charge carrier transfer [32].

The elements distribution of TP-AABR-ACK and DP-AABR-ACK composites were investigated through the energy-dispersive X-ray spectroscopy (EDX) measurement. The three elements Ag, Br, and C were distributed in the as-prepared samples, which confirmed the co-existence of AABR nanoparticles (NPs) and carbon in the samples as depicted in Figure 3a–h. In addition, a more than 1:1 molar ratio of Ag$^+$: Br$^-$ in the DP-AABR-ACK sample was observed in EDX (Figure 3a,e), which confirmed the creation of more metallic Ag NPs in the composite, compared to TP-AABR-ACK. The excessive Ag content on the surface of AgBr for DP-AABR-ACK might results in reduced photocatalytic activity [33], while TP-AABBR-ACK with low content and order dispersion of AABR nanospheres will enhance TC removal efficiently in this study [33,34]. The three-dimensional network of the ACK structure favored for uniform distribution of AABR nanoparticles in the formed nanocomposites. Both TP-AABR-ACK and DP-AABR-ACK composites (Figure 3b–h) showed homogeneous

distribution of the main elements that promotes improved photogenerated charge carriers transfer efficiency [35], and thus significantly enhances their photocatalytic activities on TC removal, as further discussed in Figure 7.
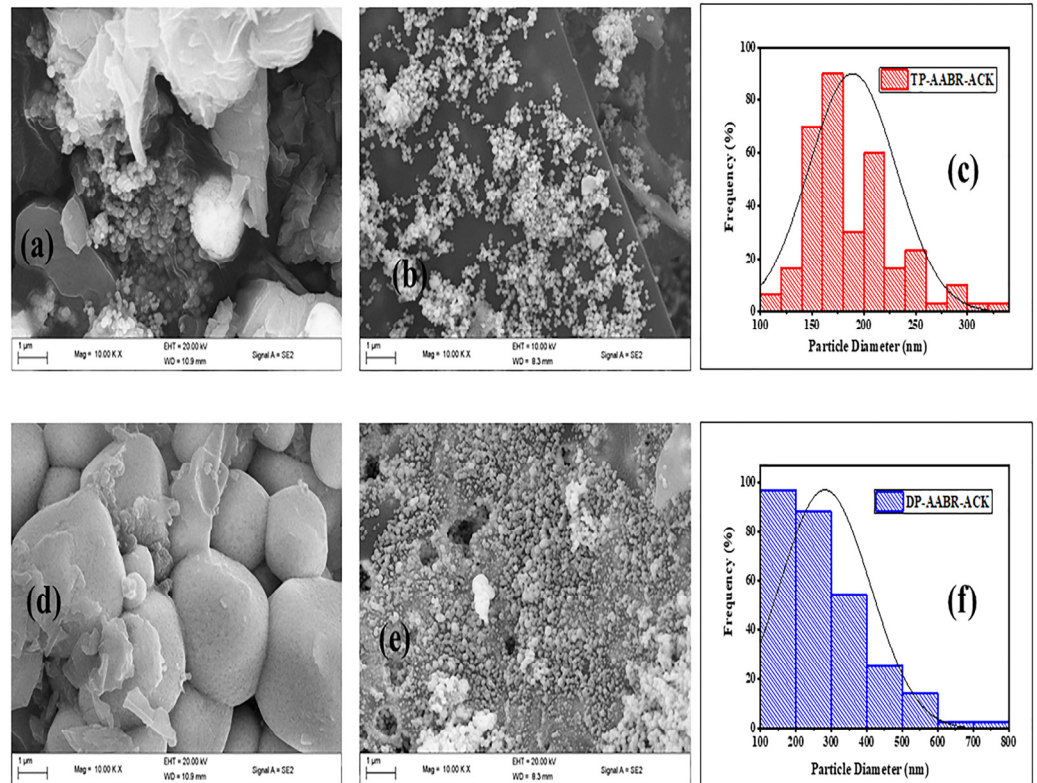

Figure 2. SEM images plasmon: (**a**) TP-AABR, (**b**) TP-AABR-ACK, (**d**) DP-AABR, (**e**) DP-AABR-ACK, and (**c**,**f**) particle size distribution of TP-AABR-ACK and DP-AABR-ACK photocatalysts.
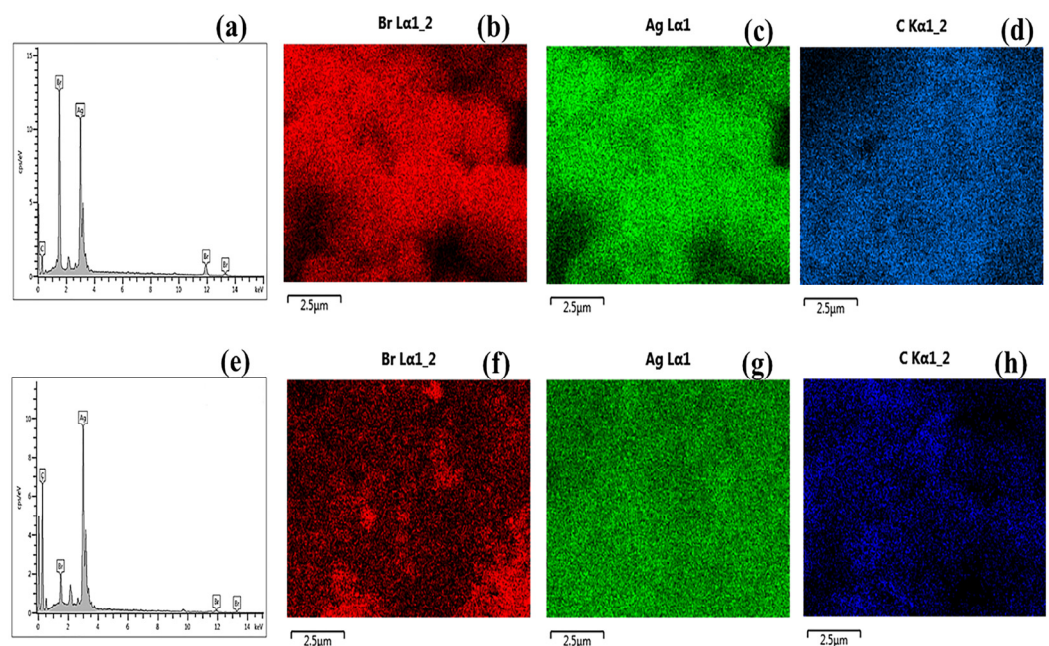

Figure 3. EDX spectrum and elemental mapping of TP-AABR-ACK (**a–d**) and DP-AABR-ACK (**e–h**).

The TEM image of TP-AAABR-ACK composite as presented in Figure 4a is nanospheres particles with particle size diameter around 3 nm (Figure 4c). The emergence of near spheres

particles with the DP-AABR-ACK is evidenced by the TEM image (Figure 4d), with particle size distribution at about 6 nm (Figure 4f). Figure 4b,e from the HRTEM image reveals d-spacing of 0.237 nm, attributed to (111) planes of metallic Ag [36], and d-spacing of 0.286 nm is assigned to (200) planes of silver bromide [37]. The particle size diameter of TP-AABR-ACK is smaller compared to the DP-AABR-ACK composite (Figure 4c,f). The TEM images for both TP-AAABR-ACK, and DP-AAABR-ACK remarkably evidenced the metallic Ag and AgBr within the nanocomposites, as their direct contact with ACK is desirable in the development of a strong heterostructure for enhanced charge carrier separation.
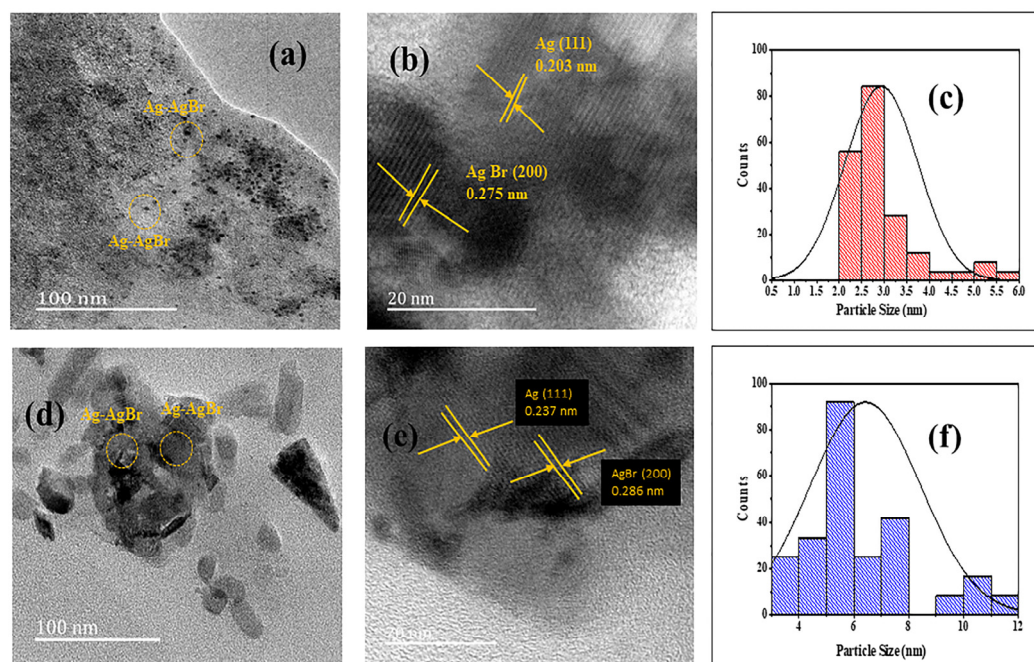

Figure 4. (**a**,**d**) Transmission electron micrographs, (**b**,**d**) high-resolution Transmission electron micrographs, and (**c**,**f**) particle diameter of the TP-AABR-ACK and DP-AABR-ACK photocatalysts.

The composites (TP-AAABR-ACK and DP-AABR-ACK) functionals groups and the presence of carbonaceous material in the composites were confirmed by FTIR measurement and presented in Figure 5. The FTIR weak band at 3405 cm^{-1} associated with weak O-H stretching vibrations of the ACK [38], while the carbonyl (-C=O) stretching band of the carboxylic groups was also observed, 1692 cm^{-1} [39], and the peak at 1575 cm^{-1} is attributed to the -C=C vibrational bond of the aromatic ring [25]. The characteristic bands of C-OH and C-O-C were also detected at 1288, 1127, and 1026 cm^{-1}, respectively, revealed the presence of ACK catalysts support within the AABR-ACK composites. However, the carbonyl stretching bands shifted to a high intensity for the synthesized photocatalysts as presented in Figure 5, which further affirms the formation of firm bonding as observed with previously reported studies [40,41], utilizing carbonaceous support in the hybridization of plasmon AABR composites. In addition, the aliphatic bands of the capped surfactants (PVP and HTAB) at 2912 and 2842 cm^{-1} appear with high and low intensity for TP-AAABR-ACK and DP-AABR-ACK [31,42]. The high intensity of aliphatic bands in TP-AAABR-ACK highlights the formation of ordered nanospheres AABR [43] with small particle diameter (as evidenced from SEM and TEM analysis in Figures 2b and 4a). Overall, reduction in the rapid growth of AABR particles, agglomeration prevention, and decrease in particle size distribution is evident for the active TP-AABR-ACK composite based on FTIR analysis (Figure 5).
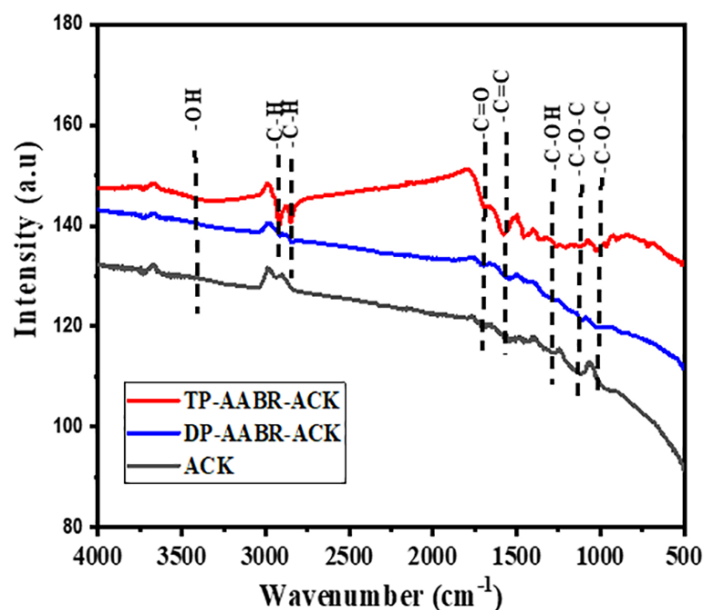
Figure 5. FTIR spectrum of ACK, DP-AABR-ACK, and TP-AABR-ACK composites.

The thermal behavior and the stability of ACK, TP-AABR-ACK, and DP-AABR-ACK/4) were investigated by thermal gravimetric analyses (TGA), and the results are presented in Figure S1. For ACK, three mass losses are evident between 30–150 °C, 150–450 °C, and 500–700 °C; which are ascribed to decomposition of adsorbed water, thermal degradation of cellulose backbone of carbon, and decomposition of extra residual carbonaceous skeleton [25,44]. The DP-AABR-ACK composite also undergoes three weight losses, as the first masses is attributed to the loss of water in the synthesized catalyst, whilst the next two occur around 230–700 °C, corresponding, respectively, to decomposition of inorganic matrixes present and extra residual carbonaceous skeleton. For TP-AABR-ACK, two main sharp decline of mass losses can be identified around 30–150 °C and 230–300 °C, as further temperature beyond 300 °C results in the sample stability, and no additional mass loss was observed. This evidenced that the TP-AABR-ACK from TP synthesis approach is critical in the controlled microstructures of AABR NPs on ACK.

The as-prepared catalysts' (TP-AABR-ACK, DP-AABR-ACK, TP-AABR, and DP-AABR) absorption strength in the visible region was investigated as presented in Figure 6a. The utilization of visible light was evident with the as-prepared catalyst, owing to the surface plasmon resonance (SPR) of metallic Ag NPs [45]. Notably, the absorption intensity for TP-AABR-ACK and DP-AABR-ACK composites increased with the addition of ACK. The 3D hierarchical structure of ACK also aids light transmittance within the TP-AABR-ACK and DP-AABR-ACK composites, thus enhancing the absorption edge of AABR for higher activity compared to TP-AABR and DP-AABR catalysts, similar to other reports [10,46,47]. However, the TP-AABR-ACK composite showed better absorption in the visible region of the solar spectrum compared to the DP-AABR-ACK catalyst, which can be ascribed to controlled microstructures (morphologies and particle size) of AABR NPs. The excessive Ag content in DP-AABR-ACK (from EDX analysis in Figure 3) will cover up the actives sites of the material, and thus reduces the visible light absorption for the generation of ROS [48,49]. The enhanced visible light response of TP-AABR-ACK with controlled microstructures will promote solar spectrum utilization in the rapid formation of photogenerated charge pairs [50], thus resulting in higher photocatalytic activity than other catalysts in this study.
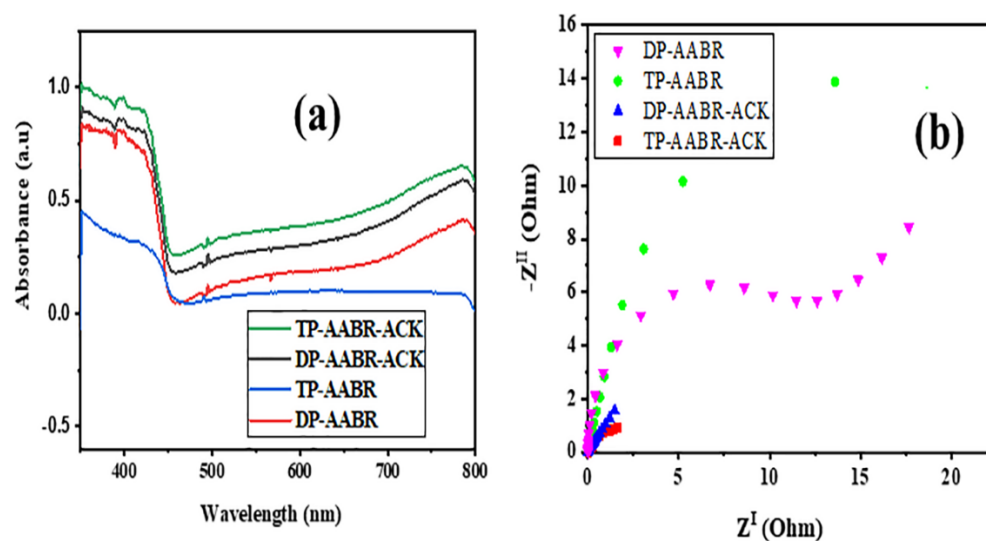
Figure 6. (**a**) UV–vis absorption spectra; and (**b**) EIS Nyquist plot of the synthesized catalysts.

The electrochemical impedance spectra (EIS) were evaluated to demonstrate the conducting attributes of DP-AABR, TP-AABR, DP-AABR-ACK, and TP-AABR-ACK catalysts as presented in Figure 6b. The corresponding EIS Nyquist plot for TP-AABR-ACK displays the smallest arc radius in comparison to other catalysts in this study (Figure 6b), which signifies a lower charge transfer resistance, thus promoting increased interfacial separation of charge carriers [35]. The ACK support significantly acts as a transport channel for the efficient separation of photo-generated charge carriers away from the AABR NPs, thus further boosting the catalytic attributes of TP-AABR-ACK in this study. TP-AABR-ACK with lower charge transfer also results in faster generation of ROS, thus enhancing TC degradation, which is ascribed to controlled morphologies, particle size distribution, and a superior cooperative effect between the AABR and ACK catalyst promoter.

The photocatalytic activities of the synthesized catalysts were assessed by the photocatalytic degradation of TC in aqueous under LED visible light irradiation as presented in Figure 7a. The TC solution without the photocatalyst degradation rate reached 14.66%. The TP-AABR and DP-AABR catalysts showed around 59.72 and 57.10% photoreduction of TC after 180 min of visible light irradiation. The TP-AABR-ACK composite degradation rate (92.08%) is better compared to DP-AABR-ACK (81.12%), which is attributed to the regular morphologies of AABR NPs with reduced particle diameter. The dispersion of regular shaped AABR NPs on ACK improves the degradation rate significantly. The excessive metallic Ag content in DP-AABR-ACK compared to TP-AABR-ACK (as evidenced from EDX analysis in Figure 3) can be a recombination center and hasten the recombination of charge carrier pair, resulting in reduced activity [49,51]. Overall, the TP-AABR-ACK photocatalytic performance was higher than that of DP-AABR-ACK, TP-AABR, DP-AABR NPs, and photolysis in the degradation of TC. The superior photocatalytic activity of the TP-AABR-ACK composite can be assigned to the formation of an effective heterojunction among the components [52]. High activity for the composite is also ascribed to the uniform dispersion of AABR nanospheres on ACK, thus increasing the contact area to visible light, and the promotion of the interfacial charge transfer process [53]. In addition, the photocatalytic degradation of CIP antibiotic and RhB dye was also carried out, as presented in Figure S2a,b. The results of CIP (10 mg/L; 150 mL) and RhB dye (5 mg/L; 150 mL) degradation under the same conditions clearly evidenced that TP-AABR-ACK composite had enhanced photocatalytic activities than other as-prepared catalysts in this study.
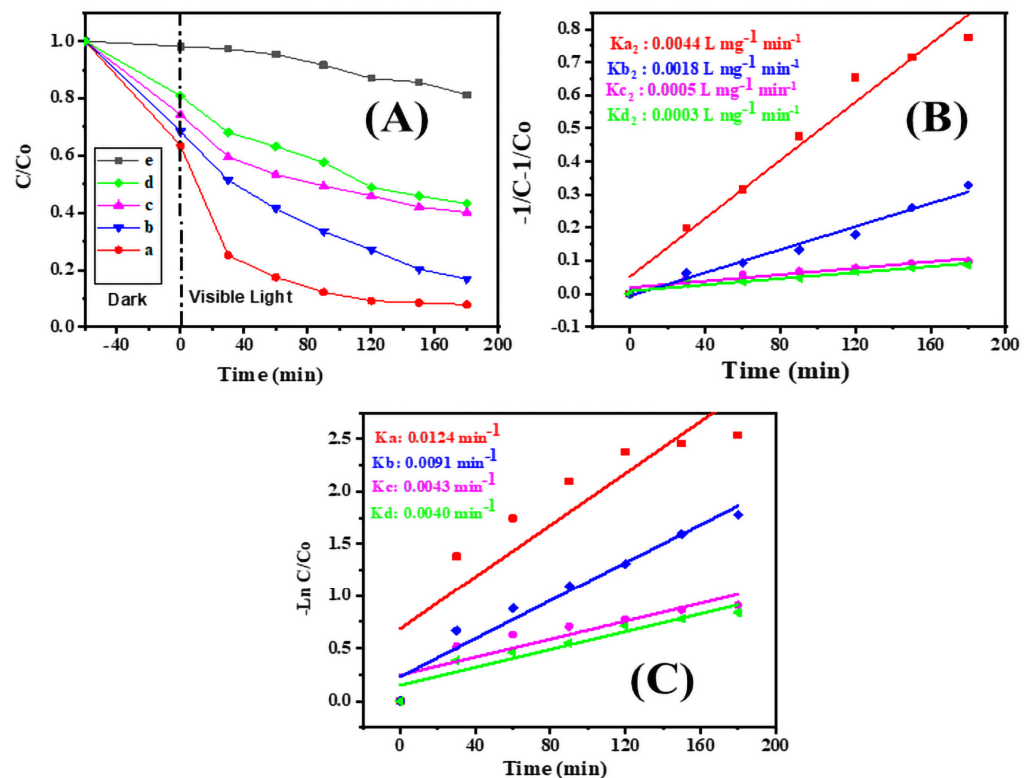
Figure 7. (**A**) Photocatalytic degradation of TC under LED visible light; (**a**) TP-AABR-ACK, (**b**) DP-AABR-ACK, (**c**) TP-AABR, (**d**) DP-AABR, and (**e**) photolysis; (**B**) second and (**C**) first order kinetics.

The photocatalytic degradation kinetics was also investigated to describe the photocatalytic rate and controlling factor for TC degradation. The kinetic data were estimated using the linearized pseudo first-order (Equation (1)) [54] and pseudo second-order models (Equation (2)) as presented below:

$$In \frac{C}{C_O} = -kt \tag{1}$$

$$\frac{1}{C} - \frac{1}{C_O} = -k_2 t \tag{2}$$

Here, t is reaction time, Co, and C are the TC concentrations at a reaction time of 0, and t min, k, and $k2$ represent the apparent rate constants for the pseudo-first order and pseudo second-order kinetics.

The pseudo second order fits the degradation of TC better compared to the pseudo first-order kinetic (Figure 7b,c). The k_{a2} value for TP-AABR-ACK (Figure 7b) is largest compared to DP-AABR-ACK, TP-AABR, and DP-AABR catalysts, respectively, in this work.

Figure 8a,b depict the UV-Vis absorption spectra of photodegraded TC over the active TP-AABR-ACK and DP-AABR-ACK composites, as a function of the time under LED visible light irradiation. The characteristic absorption band of TC antibiotic at 376 nm declines with increasing reaction time, highlighting the destruction of the aromatic ring in TC, as the intermediates were formed [42] and subsequently degraded. This analysis shows that the photocatalytic degradation efficiency of the TP-AABR-ACK is better compared to DP-AABR-ACK.

The TP-AABR-ACK and DP-AABR-ACK composites exhibit excellent photocatalytic degradation of TC in comparison with previously reported silver based photocatalysts in recent literature, as depicted in Table 1, thus justifying its potential applications in an industrial photocatalytic process.
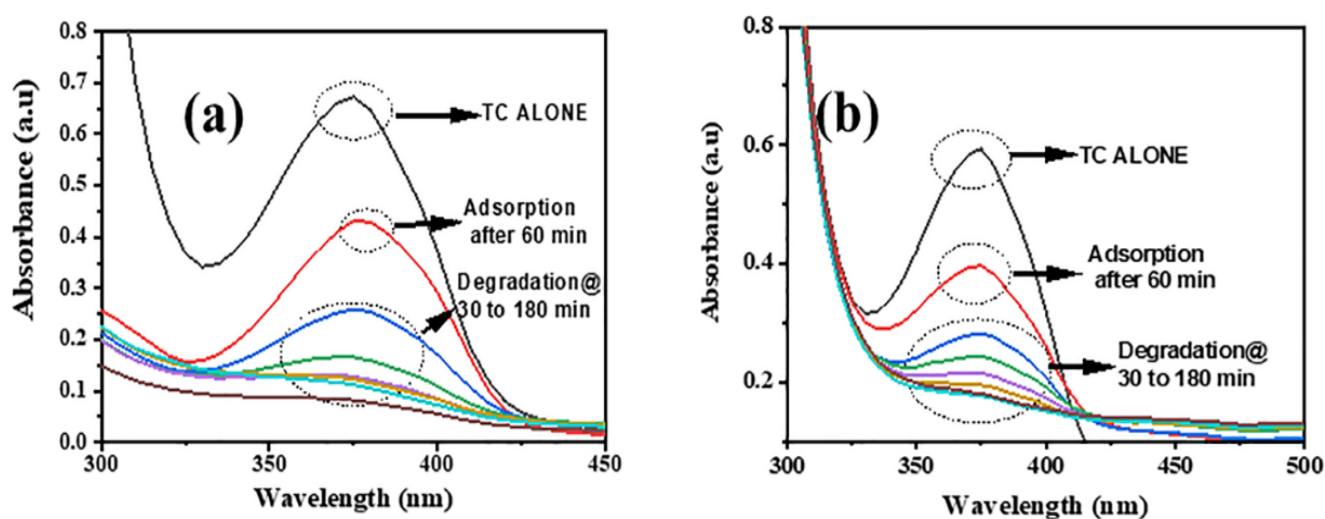
Figure 8. UV-vis absorption spectra of photodegraded TC solution using (**a**) TP-AABR-ACK and (**b**) DP-AABR-ACK.

Table 1. Comparison of degradation efficiency of different heterostructures with AABR-ACK composites on tetracycline removal.

Catalyst	Catalyst Mass (g), TC Concentration (ppm)	Light Source	% Degradation	References
Ag/AgBr/AgIn(MoO$_4$)$_2$	0.1, 10	500 W Xe lamp	42 after 40 min	[55]
AgI-WO$_3$	0.04, 35	300 W Xe lamp	75 after 60 min	[56]
Ag-K$_2$Ta$_2$O$_6$	0.1, 20	300 W Xe lamp	50 after 270 min	[57]
Ag/Bi$_3$TaO$_7$	0.05, 10	250 W Xe lamp	85 after 60 min	[58]
Ag$_2$CO$_3$/Ag/WO$_3$	0.1, 10	300 W Xe lamp	81 after 90 min	[59]
graphene-like BN/BiOBr	0.05, 20	300 W Xe lamp	75 after 80 min	[60]
GO/CN/BiOI	0.03, 20	35 W LED track light	74, after 100 min	[61]
Bi$_4$NbO$_8$Cl perovskite	0.01, 20	18-W LED bulb	79, after 60 min	[62]
TP-AABR-ACKDP-AABR-ACK	0.045, 15	36 W Visible LED Light	92 after 180 min 81 after 180 min	This Study

The recovery capacity of the active AABR-ACK nanocomposites was also researched under the LED powered visible light illumination up to five cycles, as presented in Figure S3. The degradation slightly diminishes from 91.9 to 83.27% (TP-AABR-ACK) and 81.12 to 74.14% (DP-AABR-ACK) after repeated five cycles., thus highlighting its reusability. Besides, the XRD pattern of active AABR-ACK nanocomposites after 5 cycles also affirms the stability of the synthesized composites (Figure S3b). The characteristic peaks of the photocatalysts remain unchanged, showing the good reusability of active AABR-ACK nanocomposites after the photocatalytic reaction process.

TOC Teledyne Tekmar analyzer evaluated the mineralization ability of the prepared catalysts, and their results are presented in Figure 9. The carbon content of degraded TC molecules decreased significantly, as the TP-AABR-ACK composite gave a total TOC removal efficiency of 87.5% after 180 min, which is higher compared to DP-AABR-ACK, TP-AABR, and DP-AABR (78.5%, 19%, and 15.4%) under the same conditions. This further indicates that the TP-AABR-ACK composite presents enhanced mineralization ability in TC antibiotic degradation, indicating the formation of inorganic ions, and CO$_2$. Overall, the AABR NPs uniformly decorated onto the 3D porous network ACK in the TP-AABR-ACK composite enhanced the mineralization process five-fold.
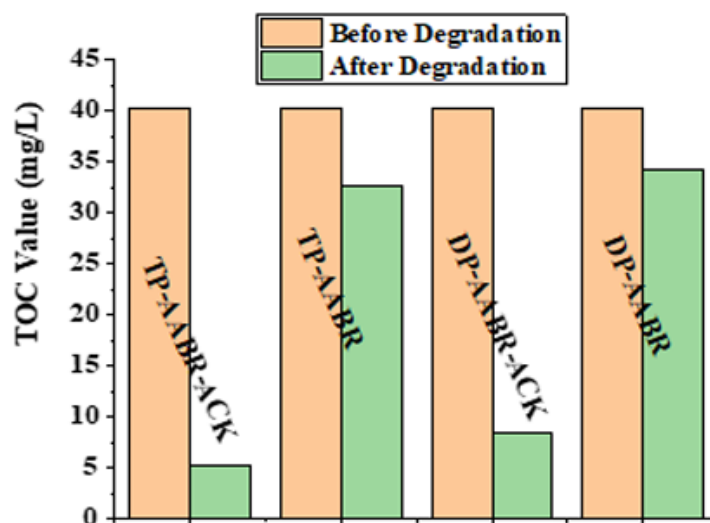
Figure 9. TOC changes of TC before and after photocatalytic reaction using as-prepared samples.

In the scavenging experiment, the degradation rate of TC significantly inhibited around 9–12%, and 29–35%, with the addition of BQ and EDTA-Na$_2$, respectively (Figure 10). The addition of IPA had a minimal contribution, while the mixture of all the scavengers highlights the ROS contribution in TC degradation in this study. The $^{\cdot}O_2^-$ significantly enhanced the TC degradation, which aligned well with previous studies [30,63]; thus, the significant role of superoxide anion radical is further explored in this study.
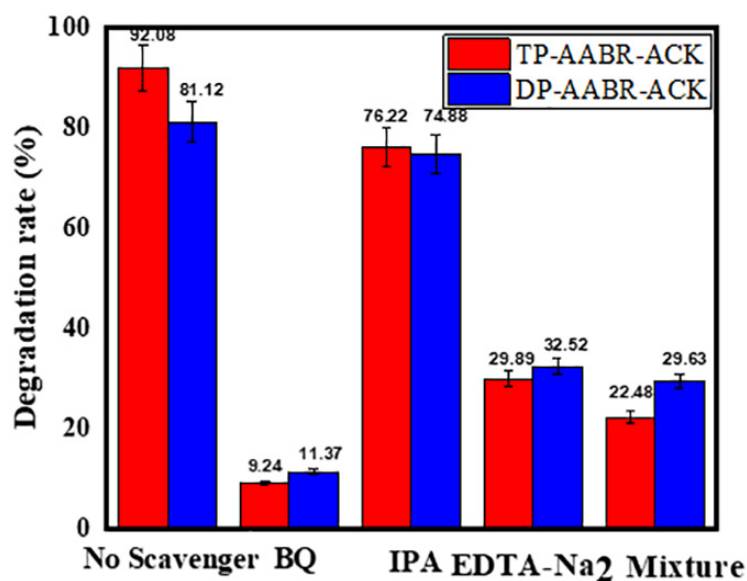

Figure 10. Photocatalytic degradation of TC solution over active AABR-ACK nanocomposites with scavenger agents.

The formation rate of superoxide anion radical ($^{\cdot}O_2^-$) through the nitroblue tetrazolium (NBT) photocatalytic degradation conversion into diformazan [64] under visible light irradiation was conducted. The production rate of $^{\cdot}O_2^-$ measured through the reduction in absorbance band of NBT molecules @259 nm is presented in Figure 11a–d. A higher amount of reactive $^{\cdot}O_2^-$ is generated more with TP-AABR-ACK composite (Figure 11d) with a rapid reduction in absorbance wavelength of NBT, which aligns with the enhanced degradation rate of TC antibiotic compared to DP-AABR-ACK, TP-AABR, and DP-AABR catalysts. Among the photocatalysts employed, the highest generation rate of a superoxide radical based on the highest NBT disappearance follows the order TP-AABR-ACK > DP-

AABR-ACK > TP-AABR > DP-AABR in this study. The enhanced production of ROS is significantly attributed with the efficient separation of the photogenerated charge carriers of the TP-AABR-ACK (as evidenced from EIS Nyquist spectra in Figure 6).
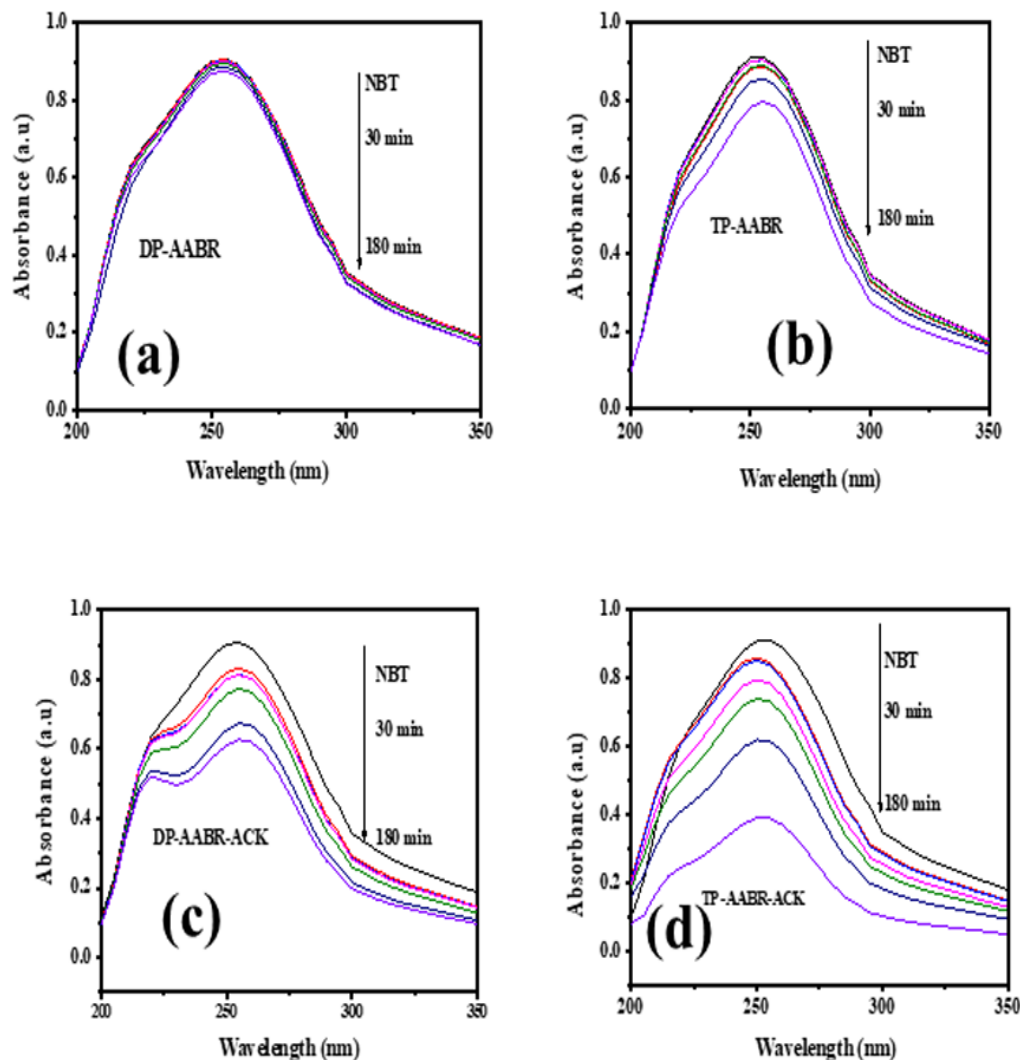

Figure 11. UV-Vis absorption spectra of NBT degraded by (**a**) DP-AABR, (**b**) TP-AABR, (**c**) DP-AABR-ACK, and (**d**) TP-AABR-ACK.

From the discussion described above, the ACK catalyst promoter/support significantly reduced aggregation and agglomeration AABR NPs, along with controlled morphologies of AABR-ACK composites, and thus promotes high interfacial separation of photogenerated charge carriers. These attributes also result in abundance generation of ROS with these composites, thus resulting in higher photocatalytic activity towards oxidative reduction of TC as depicted in Figure 7.

3. Experimental Section

3.1. Materials

Ethylene glycol (EG, 99%, Acros), polyvinylpyrrolidone (0.26 g, PVP, M.W. 58,000, K 29–32 Acros), hexadecyltrimethylammonium bromide (HTAB, Acros, 99%), silver nitrate (AgNO$_3$, Merck, Johannesburg, South Africa, 98%), nitroblue tetrazolium solution (Sigma Aldrich, St. Louis, MO, USA, 99%), *p*-benzoquinone (BQ), disodium ethylenediaminetetraacetic acid (EDTA-Na$_2$), and isopropanol (IPA) were used as received.

3.2. Activated Carbon (ACK)

Activated carbon produced from the microwave heating of impregnated pinecone biomass has been reported [25,30].

3.2.1. Preparation of TP-AABR-ACK through Thermal Polyol Route

TP-AABR-ACK was synthesized by a modified thermal polyol process [17,30]: 18 mL of EG was added into a 250 mL round-bottom flask, and further subjected to heating at 60 °C for 30 min. Polyvinylpyrrolidone (0.26 g, PVP) and 0.48 g of HTAB were sequentially added to the stirred solution, and then, 0.03 g of ACK was further added to the reaction mixture. Two hundred mg AgNO$_3$ dissolved in 3 mL EG solution in the dark was then added drop-wise into the stirred solution. The suspension was maintained at 60 °C for another 30 min, and thereafter heated to 140 °C. After reaching 140 °C, the reaction was stirred further for 18 min. Thereafter, precipitate was collected by centrifugation, washed with ethanol three times, and dried at 60 °C in an oven. TP-AABR was prepared through the above-described route, without the addition of ACK.

3.2.2. Preparation of DP-AABR-ACK through Deposition-Precipitation Route

AABR NPs composite was synthesized onto ACK catalyst support via the deposition–precipitation method [11]. In brief, 12 mL EG solution was added into a 250 mL round-bottom flask, and heated at a temperature of 65 °C for 30 min. Then, 0.26 g HTAB and 0.09 g ACK were added to the magnetically stirred solution. A defined amount of AgNO$_3$, dissolved in 1 M ammonium water 2.5 mL, was added dropwise to the stirred solution. The suspension was magnetically stirred for another 6 h under ambient light, required for the production of Ag NPs. The precipitate was collected by centrifugation, further washed with ethanol and deionized water three times, and dried in an oven at 60 °C overnight. DP-AABR was synthesized using the same route without ACK in the synthesis process.

3.3. Characterization

X-ray diffraction (XRD) patterns were obtained using a powder X-ray diffractometer (Shimadzu X-ray 700) at 40 kV and 15 mA with a Cu Kα radiation source (0.1504 nm). The morphology and elemental mapping of the synthesized photocatalyst samples were observed by the scanning electron microscopy (SEM, ZEISS Ultra/Plus FEG-SEM) with an accelerating voltage around 10–20 kV. The microstructure attributes were conducted by transmission electron microscope (TEM, JEOL JEM-2010) with an accelerating voltage of 200 kV. Fourier transform infrared spectrometer (FTIR) spectra of the samples were recorded on a Perkin Elmer spectrum 400, in the range of 600–4000 cm^{-1}. PerkinElmer STA 6000 was employed for thermal studies at a heating rate of 10 °C min^{-1} in the temperature range from 30 to 900 °C under nitrogen purge stream. Ultraviolet-visible (UV–vis) diffuse reflectance spectra were performed on a Maya 2000, Ocean Optics spectrometer using BaSO$_4$ as the reference sample. A Biologic SP 240 potentiostat workstation was utilized for electrochemical impedance spectroscopy (EIS) tests under a typical three-electrode system. A platinum wire, glassy carbon electrode, an Ag/AgCl electrode served as the counter, working, and reference electrodes, respectively.

3.4. Measurement of Photocatalytic Activity

Photocatalytic activities of the synthesized photocatalyst were evaluated by the removal efficiency of TC antibiotic with visible light irradiation. One hundred and fifty mL aqueous suspensions, containing 0.3 g/L catalyst loading of the photocatalysts, and 15 mg/L of TC, were prepared in 500 mL beaker. Before irradiation, the above-mixed solution was subjected to a dark reaction for 60 min to establish an adsorption–desorption equilibrium. Afterwards, the prepare suspension was irradiated by LED Visible light (36 W) with continuous magnetic stirring. During the photoreaction, a 3.0 mL reaction solution was collected at 30 min regular intervals and centrifuged to separate the photocatalyst. The residual TC solution was measured via a UV-vis spectrophotometer at the characteristic

absorption peak of 376 nm. Moreover, the influence of sacrificial agents comprising of *p*-benzoquinone (BQ) for superoxide ($\cdot O_2^-$), disodium ethylenediaminetetraacetic acid (EDTA-Na$_2$) for the hole (h^+), and isopropanol (IPA) for hydroxyl ($\cdot OH$) at 1 mmole, on the degradation rate of TC over most active TP-AABR-ACK and DP-AABR-ACK, was also evaluated in this study.

The recyclability experiment of our active AABR-ACK nanocomposites was examined for five cycles of TC photocatalytic degradation, utilizing 150 mL of the TC antibiotic (15 mg/L). After the initial first cycle, the photocatalyst nanocomposites were detached from the photodegraded TC solution by centrifugation and washed with distilled water to eliminate any adsorbed TC. The washed photocatalyst was then dried at room temperature, and afterward reused in the following TC degradation cycle. This process was repeated four times to acquire the five reusability cycles.

Similar to the photodegradation experiments, the measurement of superoxide radicals generated was carried out, using nitroblue tetrazolium molecules. The nitroblue tetrazolium (NBT) can be specifically reduced by the superoxide ion to form the insoluble purple formazan in the aqueous solution. A 20 mg/L Nitroblue Tetrazolium solution (Sigma Aldrich, 99%) with 0.3 g/L of photocatalysts was degraded under LED visible light, and the change in concentration was measured at a maximum absorbance wavelength of 259 nm. Total Organic Carbon (TOC) analysis was performed to determine the mineralization degree of the TC reached after the photocatalytic process.

4. Conclusions

The morphologies and particle size distributions of AABR-ACK composites (TP-AABR-ACK and DP-AABR-ACK) were controlled in this work, under the influence of two methods (thermal polyol and deposition-precipitation). TP-AABR-ACK had unique nanospheres morphologies, lower particle size, no agglomeration, thus resulting in restrained recombination of photogenerated charge carriers. The TP-AABR-ACK composite activities on TC degradation were superior to DP-AABR-ACK and corresponding AABR NPs under visible light irradiation, its exceptional morphological and conductivity properties, thus further evidenced in the TOC tests. The ACK catalyst support with interfacial interaction with AABR NPs improved the crystallinity of AABR NPs through shifting of the peaks. The ACK also boosted the light harvesting attributes of AABR NPs into the visible region for more production of ROS, and enhanced the separation of photogenerated charge carrier in the catalytic process. In addition, the TP-AABR-ACK nanocomposite is capable of producing abundant ROS (superoxide anions radicals), compared to DP-AABR-ACK, occurring through the intrinsic interactive reaction of nitroblue tetrazolium molecules with the active TP-AABR-ACK.

Data Availability Statement: The data presented in this study are openly available in the University of Pretoria Research Data Repository at DOI: 10.25403/UPresearchdata.17038907.

Conflicts of Interest: The authors declare no conflict of interest.

References

1. Zhang, H.; Liu, P.; Feng, Y.; Yang, F. Fate of antibiotics during wastewater treatment and antibiotic distribution in the effluent-receiving waters of the Yellow Sea, northern China. *Mar. Poll. Bull.* **2013**, *73*, 282–290. [CrossRef]
2. Fernandes, A.; Oliveira, C.; Pacheco, M.J.; Ciríaco, L.; Lopes, A. Anodic oxidation of oxytetracycline: Influence of the experimental conditions on the degradation rate and mechanism. *J. Electrochem. Sci. Eng.* **2014**, *4*, 203–213. [CrossRef]
3. Zhu, Y.; Han, Z.; Zhao, S.; Zhang, Q.; Shen, X.; Lv, H.; Liu, J.; Li, B. In-situ growth of Ag/AgBr nanoparticles on a metal organic framework with enhanced visible light photocatalytic performance. *Mater. Sci. Semicond. Process.* **2021**, *133*, 105973. [CrossRef]
4. Chao, Y.; Zhu, W.; Yan, B.; Lin, Y.; Xun, S.; Ji, H.; Wu, X.; Li, H.; Han, C. Macroporous polystyrene resins as adsorbents for the removal of tetracycline antibiotics from an aquatic environment. *J. Appl. Polym. Sci.* **2014**, *131*, 40561. [CrossRef]
5. Yao, Y.; Zhang, Y.; Shen, M.; Li, W.; Xia, W. The facile synthesis and enhanced photocatalytic properties of ZnO@ ZnS modified with Ag0 via in-situ ion exchange. *Colloids. Surf. A Physicochem. Eng. Aspects* **2020**, *591*, 124556. [CrossRef]
6. Fang, Y.; Li, Y.; Zhou, F.; Gu, P.; Liu, J.; Chen, D.; Li, N.; Xu, Q.; Lu, J. An Efficient Photocatalyst Based on Black TiO$_2$ Nanoparticles and Porous Carbon with High Surface Area: Degradation of Antibiotics and Organic Pollutants in Water. *Chem. Plus Chem.* **2019**, *84*, 474–480.
7. Zhao, X.; Lu, Z.; Wei, M.; Zhang, M.; Dong, H.; Yi, C.; Ji, R.; Yan, Y. Synergetic effect of carbon sphere derived from yeast with magnetism and cobalt oxide nanochains towards improving photodegradation activity for various pollutants. *Appl. Catal. B Environ.* **2018**, *220*, 137–147. [CrossRef]
8. Ye, Y.; Zang, Z.; Zhou, T.; Dong, F.; Lu, S.; Tang, X.; Wei, W.; Zhang, Y. Theoretical and experimental investigation of highly photocatalytic performance of CuInZnS nanoporous structure for removing the NO gas. *J. Catal.* **2018**, *357*, 100–107. [CrossRef]
9. Bhachu, D.S.; Moniz, S.J.; Sathasivam, S.; Scanlon, D.O.; Walsh, A.; Bawaked, S.M.; Mokhtar, M.; Obaid, A.Y.; Parkin, I.P.; Tang, J. Bismuth oxyhalides: Synthesis, structure and photoelectrochemical activity. *Chem. Sci.* **2016**, *7*, 4832–4841. [CrossRef]
10. Bano, Z.; Saeed, R.Y.; Zhu, S.; Xia, M.; Mao, S.; Lei, W.; Wang, F. Mesoporous CuS nanospheres decorated rGO aerogel for high photocatalytic activity towards Cr (VI) and organic pollutants. *Chemosphere* **2020**, *246*, 125846. [CrossRef] [PubMed]
11. Zhu, M.; Chen, P.; Liu, M. High-performance visible-light-driven plasmonic photocatalysts Ag/AgCl with controlled size and shape using graphene oxide as capping agent and catalyst promoter. *Langmuir* **2013**, *29*, 9259–9268. [CrossRef]
12. Yan, T.; Zhang, H.; Luo, Q.; Ma, Y.; Lin, H.; You, J. Controllable synthesis of plasmonic Ag/AgBr photocatalysts by a facile one-pot solvothermal route. *Chem. Eng. J.* **2013**, *232*, 564–572. [CrossRef]
13. Errokh, A.; Cheikhrouhou, W.; Ferraria, A.M.; do Rego, A.M.B.; Boufi, S. Cotton decorated with Cu$_2$O-Ag and Cu$_2$O-Ag-AgBr NPs via an in-situ sacrificial template approach and their antibacterial efficiency. *Colloids Surf. B Biointerface* **2021**, *200*, 111600. [CrossRef] [PubMed]
14. Cao, D.; Wang, Q.; Liu, Z.; Zhang, H.; Wang, Y.; Jin, R.; Gao, S. Enhanced the photoelectrocatalytic performance of TiO$_2$ nanotube arrays by the synergistic sensitization of Ag–AgBr nanospheres. *Spectrochim. Acta Part A Mol. Biomol. Spectrosc.* **2020**, *227*, 117674. [CrossRef] [PubMed]
15. Xiao, J.-Q.; Lin, K.-S.; Yu, Y. Novel Ag@ AgCl@ AgBr heterostructured nanotubes as high-performance visible-light photocatalysts for decomposition of dyes. *Catal. Today* **2018**, *314*, 10–19. [CrossRef]
16. Li, B.; Wang, H.; Zhang, B.; Hu, P.; Chen, C.; Guo, L. Facile synthesis of one dimensional AgBr@ Ag nanostructures and their visible light photocatalytic properties. *ACS Appl. Mater. Interface* **2013**, *5*, 12283–12287. [CrossRef] [PubMed]
17. Chen, G.; Li, F.; Huang, Z.; Guo, C.-Y.; Qiao, H.; Qiu, X.; Wang, Z.; Jiang, W.; Yuan, G. Facile synthesis of Ag/AgBr/RGO nanocomposite as a highly efficient sunlight plasmonic photocatalyst. *Catal. Commun.* **2015**, *59*, 140–144. [CrossRef]
18. Xu, X.; Shen, X.; Zhou, H.; Qiu, D.; Zhu, G.; Chen, K. Facile microwave-assisted synthesis of monodispersed ball-like Ag@ AgBr photocatalyst with high activity and durability. *Appl. Catal. A Gen.* **2013**, *455*, 183–192. [CrossRef]
19. Parale, V.G.; Kim, T.; Phadtare, V.D.; Yadav, H.M.; Park, H.-H. Enhanced photocatalytic activity of a mesoporous TiO$_2$ aerogel decorated onto three-dimensional carbon foam. *J. Mol. Liq.* **2019**, *277*, 424–433. [CrossRef]
20. Li, G.; Huang, B.; Pan, Z.; Su, X.; Shao, Z.; An, L. Advances in three-dimensional graphene-based materials: Configurations, preparation and application in secondary metal (Li, Na, K, Mg, Al)-ion batteries. *Energy Environ. Sci.* **2019**, *12*, 2030–2053. [CrossRef]
21. Ananthanarayanan, A.; Wang, X.; Routh, P.; Sana, B.; Lim, S.; Kim, D.H.; Lim, K.H.; Li, J.; Chen, P. Facile synthesis of graphene quantum dots from 3D graphene and their application for Fe^{3+} sensing. *Adv. Funct. Mater.* **2014**, *24*, 3021–3026. [CrossRef]
22. Che, H.; Che, G.; Zhou, P.; Liu, C.; Dong, H. Yeast-derived carbon sphere as a bridge of charge carriers towards to enhanced photocatalytic activity of 2D/2D Cu$_2$WS$_4$/g-C$_3$N$_4$ heterojunction. *J. Colloid Interface Sci.* **2019**, *546*, 262–275. [CrossRef] [PubMed]
23. Zhou, X.; Zhou, S.; Ma, F.; Xu, Y. Synergistic effects and kinetics of rGO-modified TiO$_2$ nanocomposite on adsorption and photocatalytic degradation of humic acid. *J. Environ. Manag.* **2019**, *235*, 293–302. [CrossRef] [PubMed]
24. Xu, P.; Cen, C.; Zheng, M.; Wang, Y.; Wu, Z.; Teng, Z. A facile electrostatic droplets assisted synthesis of copper nanoparticles embedded magnetic carbon microspheres for highly effective catalytic reduction of 4-nitrophenol and Rhodamine B. *Mater. Chem. Phys.* **2020**, *253*, 123444. [CrossRef]

25. Sanni, S.; Viljoen, E.; Ofomaja, A. Three-dimensional hierarchical porous carbon structure derived from pinecone as a potential catalyst support in catalytic remediation of antibiotics. *RSC Adv.* **2020**, *10*, 8717–8728. [CrossRef]

26. Fu, Y.; Xu, P.; Huang, D.; Zeng, G.; Lai, C.; Qin, L.; Li, B.; He, J.; Yi, H.; Cheng, M. Au nanoparticles decorated on activated coke via a facile preparation for efficient catalytic reduction of nitrophenols and azo dyes. *Appl. Surf. Sci.* **2019**, *473*, 578–588. [CrossRef]

27. Zhu, Q.; Wang, W.-S.; Lin, L.; Gao, G.-Q.; Guo, H.-L.; Du, H.; Xu, A.-W. Facile synthesis of the novel Ag_3VO_4/AgBr/Ag plasmonic photocatalyst with enhanced photocatalytic activity and stability. *J. Phys. Chem. C* **2013**, *117*, 5894–5900. [CrossRef]

28. Lou, Z.; Huang, B.; Qin, X.; Zhang, X.; Cheng, H.; Liu, Y.; Wang, S.; Wang, J.; Dai, Y. One-step synthesis of AgCl concave cubes by preferential overgrowth along <111> and <110> directions. *Chem. Commun.* **2012**, *48*, 3488–3490. [CrossRef]

29. Lin, Z.; Xiao, J.; Yan, J.; Liu, P.; Li, L.; Yang, G. Ag/AgCl plasmonic cubes with ultrahigh activity as advanced visible-light photocatalysts for photodegrading dyes. *J. Mater. Chem. A* **2015**, *3*, 7649–7658. [CrossRef]

30. Sanni, S.; Viljoen, E.; Ofomaja, A. Accelerated electron transport and improved photocatalytic activity of Ag/AgBr under visible light irradiation based on conductive carbon derived biomass. *Catal. Lett.* **2019**, *149*, 3027–3040. [CrossRef]

31. Sanni, S.; Viljoen, E.; Ofomaja, A. Tailored synthesis of Ag/AgBr nanostructures coupled activated carbon with intimate interface interaction for enhanced photodegradation of tetracycline. *Process Saf. Environ. Prot.* **2021**, *146*, 20–34. [CrossRef]

32. He, J.; Yang, J.; Jiang, F.; Liu, P.; Zhu, M. Photo-assisted peroxymonosulfate activation via 2D/2D heterostructure of Ti_3C_2/g-C_3N_4 for degradation of diclofenac. *Chemosphere* **2020**, *258*, 127339. [CrossRef]

33. Guo, H.; Niu, C.-G.; Wen, X.-J.; Zhang, L.; Liang, C.; Zhang, X.-G.; Guan, D.-L.; Tang, N.; Zeng, G.-M. Construction of highly efficient and stable ternary $AgBr/Ag/PbBiO_2Br$ Z-scheme photocatalyst under visible light irradiation: Performance and mechanism insight. *J. Colloid Interface Sci.* **2018**, *513*, 852–865. [CrossRef]

34. Zhang, Y.; Tang, Z.-R.; Fu, X.; Xu, Y.-J. Nanocomposite of Ag–AgBr–TiO_2 as a photoactive and durable catalyst for degradation of volatile organic compounds in the gas phase. *App. Catal. B Environ.* **2011**, *106*, 445–452. [CrossRef]

35. He, F.; Wang, Z.; Li, Y.; Peng, S.; Liu, B. The nonmetal modulation of composition and morphology of g-C_3N_4-based photocatalysts. *App. Catal. B Environ.* **2020**, *269*, 118828. [CrossRef]

36. Madigasekara, I.H.K.; Perera, H.C.S.; Kumari, J.M.K.W.; Senadeera, G.K.R.; Dissanayake, M.A.K.L. Photoanode modification of dye-sensitized solar cells with Ag/AgBr/TiO_2 nanocomposite for enhanced cell efficiency. *Sol. Energy* **2021**, *230*, 59–72. [CrossRef]

37. Sui, Y.; Su, C.; Yang, X.; Hu, J.; Lin, X. Ag-AgBr nanoparticles loaded on TiO_2 nanofibers as an efficient heterostructured photocatalyst driven by visible light. *J. Mol. Catal. A Chem.* **2015**, *410*, 226–234. [CrossRef]

38. López-Peñalver, J.J.; Sánchez-Polo, M.; Gómez-Pacheco, C.V.; Rivera-Utrilla, J. Photodegradation of tetracyclines in aqueous solution by using UV and UV/H_2O_2 oxidation processes. *J. Chem. Technol. Biotechnol.* **2010**, *85*, 1325–1333. [CrossRef]

39. Feng, Y.; Zhou, H.; Liu, G.; Qiao, J.; Wang, J.; Lu, H.; Yang, L.; Wu, Y. Methylene blue adsorption onto swede rape straw (Brassica napus L.) modified by tartaric acid: Equilibrium, kinetic and adsorption mechanisms. *Bioresour. Technol.* **2012**, *125*, 138–144. [CrossRef] [PubMed]

40. Petroski, J.; El-Sayed, M.A. FTIR study of the adsorption of the capping material to different platinum nanoparticle shapes. *J. Phys. Chem. A* **2003**, *107*, 8371–8375. [CrossRef]

41. Zhu, M.; Chen, P.; Liu, M. Graphene oxide enwrapped Ag/AgX (X = Br, Cl) nanocomposite as a highly efficient visible-light plasmonic photocatalyst. *ACS Nano* **2011**, *5*, 4529–4536. [CrossRef] [PubMed]

42. Sanni, S.; Viljoen, E.; Ofomaja, A. Design of ordered Ag/AgBr nanostructures coupled activated carbon with enhanced charge carriers separation efficiency for photodegradation of tetracycline under visible light. *J. Mol. Liq.* **2020**, *299*, 112032. [CrossRef]

43. Attia, Y.A.; Mohamed, Y.M.A. Silicon-grafted Ag/AgX/rGO nanomaterials (X = Cl or Br) as dip-photocatalysts for highly efficient p-nitrophenol reduction and paracetamol production. *Appl. Organomet. Chem.* **2019**, *33*, e4757. [CrossRef]

44. Singh, Y.D.; Mahanta, P.; Bora, U. Comprehensive characterization of lignocellulosic biomass through proximate, ultimate and compositional analysis for bioenergy production. *Renew. Energy* **2017**, *103*, 490–500. [CrossRef]

45. Jiang, J.; Li, H.; Zhang, L. New insight into daylight photocatalysis of AgBr@ Ag: Synergistic effect between semiconductor photocatalysis and plasmonic photocatalysis. *Chem. A Eur. J.* **2012**, *18*, 6360–6369. [CrossRef] [PubMed]

46. Sanni, S.; Modise, S.; Viljoen, E.; Ofomaja, A. Enhanced degradation of dye mixtures: Physicochemical and electrochemical properties of titania dispersed on clinoptilolite, synergistic influence. *SN Appl. Sci.* **2020**, *2*, 1–10. [CrossRef]

47. Wang, H.; Liu, H.; Wang, S.; Li, L.; Liu, X. Influence of tunable pore size on photocatalytic and photoelectrochemical performances of hierarchical porous TiO_2/C nanocomposites synthesized via dual-Templating. *Appl. Catal. B Environ.* **2018**, *224*, 341–349. [CrossRef]

48. Bhatt, D.K.; Patel, U.D. Mechanism underlying visible-light photocatalytic activity of Ag/AgBr: Experimental and theoretical approaches. *J. Phys. Chem. Solids* **2019**, *135*, 109118. [CrossRef]

49. Deng, F.; Zhao, L.; Luo, X.; Luo, S.; Dionysiou, D.D. Highly efficient visible-light photocatalytic performance of Ag/$AgIn_5S_8$ for degradation of tetracycline hydrochloride and treatment of real pharmaceutical industry wastewater. *Chem. Eng. J.* **2018**, *333*, 423–433. [CrossRef]

50. Soltani, T.; Tayyebi, A.; Lee, B.-K. Photolysis and photocatalysis of tetracycline by sonochemically heterojunctioned $BiVO_4$/reduced graphene oxide under visible-light irradiation. *J. Environ. Manag.* **2019**, *232*, 713–721. [CrossRef]

51. Hu, P.; Cao, Y.J.D.T. A new chemical route to a hybrid nanostructure: Room-temperature solid-state reaction synthesis of Ag@ AgCl with efficient photocatalysis. *Dalton Trans.* **2012**, *41*, 8908–8912. [CrossRef]

52. Ren, Y.; Dong, T.; Ding, S.; Liu, X.; Zheng, H.; Gao, L.; Hu, J. AgBr Nanoparticles Anchored on CdS Nanorods as Photocatalysts for H2 Evolution. *ACS Appl. Nano Mater.* **2021**, *4*, 9274–9282. [CrossRef]

53. De Moraes, N.P.; Valim, R.B.; da Silva Rocha, R.; da Silva, M.L.C.P.; Campos, T.M.B.; Thim, G.P.; Rodrigues, L.A. Effect of synthesis medium on structural and photocatalytic properties of ZnO/carbon xerogel composites for solar and visible light degradation of 4-chlorophenol and bisphenol A. *Colloids Surf. A Physicochem. Eng. Asp.* **2020**, *584*, 124034. [CrossRef]

54. Xu, J.; Wang, W.; Shang, M.; Sun, S.; Ren, J.; Zhang, L. Efficient visible light induced degradation of organic contaminants by Bi$_2$WO$_6$ film on SiO$_2$ modified reticular substrate. *Appl. Catal. B Environ.* **2010**, *93*, 227–232. [CrossRef]

55. Yan, X.; Wang, X.; Gu, W.; Wu, M.; Yan, Y.; Hu, B.; Che, G.; Han, D.; Yang, J.; Fan, W. Single-crystalline AgIn (MoO$_4$)$_2$ nanosheets grafted Ag/AgBr composites with enhanced plasmonic photocatalytic activity for degradation of tetracycline under visible light. *Appl. Catal. B Environ.* **2015**, *164*, 297–304. [CrossRef]

56. Xu, D.; Liu, K.; Shi, W.; Chen, M.; Luo, B.; Xiao, L.; Gu, W. Ag-decorated K$_2$Ta$_2$O$_6$ nanocomposite photocatalysts with enhanced visible-light-driven degradation activities of tetracycline (TC). *Ceram. Int.* **2015**, *41*, 4444–4451. [CrossRef]

57. Yang, S.-F.; Niu, C.-G.; Huang, D.-W.; Zhang, H.; Zeng, G.-M. Ag/AgCl nanoparticles-modified CdSnO$_3$·3H$_2$O nanocubes photocatalyst for the degradation of methyl orange and antibiotics under visible light irradiation. *J. Colloid Interface Sci.* **2017**, *505*, 96–104. [CrossRef] [PubMed]

58. Yuan, X.; Jiang, L.; Chen, X.; Leng, L.; Wang, H.; Wu, Z.; Xiong, T.; Liang, J.; Zeng, G. Highly efficient visible-light-induced photoactivity of Z-scheme Ag$_2$CO$_3$/Ag/WO$_3$ photocatalysts for organic pollutant degradation. *Environ. Sci. Nano* **2017**, *4*, 2175–2185. [CrossRef]

59. Wang, T.; Quan, W.; Jiang, D.; Chen, L.; Li, D.; Meng, S.; Chen, M. Synthesis of redox-mediator-free direct Z-scheme AgI/WO 3 nanocomposite photocatalysts for the degradation of tetracycline with enhanced photocatalytic activity. *Chem. Eng. J.* **2016**, *300*, 280–290. [CrossRef]

60. Di, J.; Xia, J.; Ji, M.; Wang, B.; Yin, S.; Zhang, Q.; Chen, Z.; Li, H. Advanced photocatalytic performance of graphene-like BN modified BiOBr flower-like materials for the removal of pollutants and mechanism insight. *Appl. Catal. B Environ.* **2016**, *183*, 254–262. [CrossRef]

61. Wang, Q.; Li, Y.; Huang, L.; Zhang, F.; Wang, H.; Wang, C.; Zhang, Y.; Xie, M.; Li, H. Enhanced photocatalytic degradation and antibacterial performance by GO/CN/BiOI composites under LED light. *Appl. Surf. Sci.* **2019**, *497*, 143753. [CrossRef]

62. Majumdar, A.; Pal, A. Optimized synthesis of Bi$_4$NbO$_8$Cl perovskite nanosheets for enhanced visible light assisted photocatalytic degradation of tetracycline antibiotics. *J. Environ. Chem. Eng.* **2020**, *8*, 103645. [CrossRef]

63. Zhang, T.; Yin, Q.; Zhang, M.; Zhang, S.; Shao, Y.; Fang, L.; Yan, Q.; Sun, X. Enhanced photocatalytic activity of AgBr photocatalyst via constructing heterogeneous junctions with reduced graphene. *J. Mater. Sci. Mater. Electron.* **2021**, *32*, 15331–15342. [CrossRef]

64. Obregón, S.; Zhang, Y.; Colón, G. Cascade charge separation mechanism by ternary heterostructured BiPO$_4$/TiO$_2$/gC$_3$N$_4$ photocatalyst. *Appl. Catal. B Environ.* **2016**, *184*, 96–103. [CrossRef]